

# Melt network reorientation and crystallographic preferred orientation development in sheared partially molten rocks

Cassandra Seltzer<sup>1</sup>, Matěj Peč<sup>2</sup>, Mark E. Zimmerman<sup>3</sup>, and David L Kohlstedt<sup>3</sup>

<sup>1</sup>Massachusetts Institute of Technology

<sup>2</sup>MIT EAPS

<sup>3</sup>University of Minnesota

February 27, 2023

## Abstract

As partially molten rocks deform, they develop melt preferred orientations, shape preferred orientations, and crystallographic preferred orientations (MPOs, SPOs and CPOs). We investigated the co-evolution of these preferred orientations in experimentally deformed partially molten rocks, then calculated the influence of MPO and CPO on seismic anisotropy. Olivine-basalt aggregates containing 2 to 4 wt% melt were deformed in general shear at a temperature of 1250°C under a confining pressure of 300 MPa at shear stresses of  $\tau = 0$  to 175 MPa to shear strains of  $\gamma = 0$  to 2.3. Grain-scale melt pockets developed a MPO parallel to the maximum principal stress,  $s_1$ , at  $\gamma < 0.4$ . At higher strains, the grain-scale MPO remained parallel to  $s_1$ , but incipient, sample-scale melt bands formed at  $\sim 20^\circ$  to  $s_1$ . An initial SPO and CPO were induced during sample preparation, with [100] and [001] axes girdled perpendicular to the long axis of the sample. At the highest explored strain, a strong SPO was established, and the [100] axes of the CPO clustered nearly parallel to the shear plane. Our results demonstrate that grain-scale and sample-scale alignments of melt pockets are distinct. Furthermore, the melt and the solid microstructures evolve on different timescales: in planetary bodies, changes in the stress field will first drive a relatively rapid reorientation of the melt network, followed by a relatively slow realignment of the crystallographic axes. Rapid changes to seismic anisotropy in a deforming partially molten aggregate are thus caused by MPO rather than CPO.

## Hosted file

957019\_0\_art\_file\_10738493\_rqjvn7.docx available at <https://authorea.com/users/589742/articles/626431-melt-network-reorientation-and-crystallographic-preferred-orientation-development-in-sheared-partially-molten-rocks>

1  
2  
3  
4  
5  
6  
7  
8  
9  
10  
11  
12  
13  
14  
15  
16  
17  
18  
19  
20  
21  
22  
23  
24

Melt network reorientation and crystallographic preferred orientation development in sheared partially molten rocks

C. Seltzer<sup>1</sup>, M. Peč<sup>1</sup>, M.E. Zimmerman<sup>2</sup>, D.L. Kohlstedt<sup>2</sup>

<sup>1</sup>Department of Earth, Atmospheric and Planetary Sciences, Massachusetts Institute of Technology, Cambridge, MA-02139

<sup>2</sup>Department of Earth and Environmental Sciences, University of Minnesota, Minneapolis, MN-55455

Corresponding author: Cassandra Seltzer (cseltz@mit.edu)

#### Key Points

1. The melt network in a deforming partially molten rock responds more quickly to a changing stress field than do its crystalline axes.
2. Grain-scale melt preferred orientation forms parallel to the maximum principal stress at the onset of deformation.
3. Rapid changes to seismic anisotropy observed in a deforming partially molten rock can be attributed to reorientation of melt.

25

26 **Abstract:**

27 As partially molten rocks deform, they develop melt preferred orientations, shape  
28 preferred orientations, and crystallographic preferred orientations (MPOs, SPOs and CPOs). We  
29 investigated the co-evolution of these preferred orientations in experimentally deformed partially  
30 molten rocks, then calculated the influence of MPO and CPO on seismic anisotropy. Olivine-  
31 basalt aggregates containing 2 to 4 wt% melt were deformed in general shear at a temperature of  
32 1250°C under a confining pressure of 300 MPa at shear stresses of  $\tau = 0$  to 175 MPa to shear  
33 strains of  $\gamma = 0$  to 2.3. Grain-scale melt pockets developed a MPO parallel to the maximum  
34 principal stress,  $\sigma_1$ , at  $\gamma < 0.4$ . At higher strains, the grain-scale MPO remained parallel to  $\sigma_1$ , but  
35 incipient, sample-scale melt bands formed at  $\sim 20^\circ$  to  $\sigma_1$ . An initial SPO and CPO were induced  
36 during sample preparation, with [100] and [001] axes girdled perpendicular to the long axis of  
37 the sample. At the highest explored strain, a strong SPO was established, and the [100] axes of  
38 the CPO clustered nearly parallel to the shear plane. Our results demonstrate that grain-scale and  
39 sample-scale alignments of melt pockets are distinct. Furthermore, the melt and the solid  
40 microstructures evolve on different timescales: in planetary bodies, changes in the stress field  
41 will first drive a relatively rapid reorientation of the melt network, followed by a relatively slow  
42 realignment of the crystallographic axes. Rapid changes to seismic anisotropy in a deforming  
43 partially molten aggregate are thus caused by MPO rather than CPO.

44

45

46

## 47 Plain language summary:

48 We studied the influence of melt alignment and crystal alignment on the properties of partially  
49 melted regions in planetary bodies. Molten and crystalline elements within the rocks in these  
50 layers can deform and reorient in response to stress, but it is difficult to predict exactly how the  
51 realignment of each phase affects seismic properties of the rocks. Reorientation of melt  
52 networks during deformation of partially molten rocks is not well constrained, as experiments  
53 and computational models disagree on the most favorable alignment of melt pockets. Here, we  
54 measured the angles and shapes of melt and crystals in experimentally deformed partially molten

55 rocks, then calculated seismic properties of the deformed rocks. We found that melt pockets  
56 change orientation and shape quickly, but crystals take longer to reorient. This indicates that  
57 immediate changes to seismic properties after a sudden change in stress field are caused by melt,  
58 rather than by crystals. We also discovered that experimental observations and modeling  
59 predictions of melt orientations do agree, but only at small scales. Our results show that when  
60 stress fields abruptly change in Earth and other planetary bodies, melt pocket orientations will  
61 control seismic properties and are the best instantaneous indicators of these stress changes.

62

63

64

## 65 **1. Introduction**

66 Partial melting often occurs alongside sites of rapid deformation in Earth's lithosphere. In  
67 response to deformation, the molten and crystalline components of partially molten rocks align,  
68 leading to anisotropies in mechanical, transport, and seismic properties (Blackman & Kendall,  
69 1997; Daines & Kohlstedt, 1997; Holtzman et al., 2003; Holtzman & Kendall, 2010; Long &  
70 Becker, 2010; Savage, 1999; Taylor-West & Katz, 2015). The interpretation of seismic images  
71 obtained from deforming partially molten regions of Earth is, however, not straightforward.  
72 Seismic waves propagating through partially molten rocks are sensitive to the bulk and shear  
73 moduli, which are determined by the poroelastic properties of the skeletal network of solid grains  
74 and the viscous properties and geometry of the interstitial melt phase (Holtzman & Kendall,  
75 2010; Mainprice, 1997; Takei, 2001). As molten and solid rock components have distinct seismic  
76 properties, the orientations of both phases contribute to the seismic anisotropy observed in  
77 Earth's upper mantle and crust (Almqvist & Mainprice, 2017; Hansen et al., 2021).

78 Experiments provide an important benchmark for melt and crystallographic preferred  
79 orientations in deformed partially molten mantle rocks. However, experimental results and  
80 modeling assumptions often disagree on the orientation of the melt network. Previous  
81 experimental studies report an alignment of the long axes of melt pockets at  $20^\circ$  to the direction  
82 of the maximum principal stress (Zimmerman et al., 1999) and, with increasing strain, the  
83 formation of melt-rich "bands" at a similar orientation (Holtzman et al., 2003; King et al., 2010).  
84 In contrast, some viscoelastic models and theories predict grain-scale melt alignment parallel to

85 the direction of the maximum principal stress,  $\sigma_1$ . (Hier-Majumder, 2011; Takei & Holtzman,  
86 2009c; Taylor-West & Katz, 2015). To resolve differences between modeling and experimental  
87 results, we reexamined microstructures of deformed partially molten samples at both the grain  
88 scale and the sample scale.

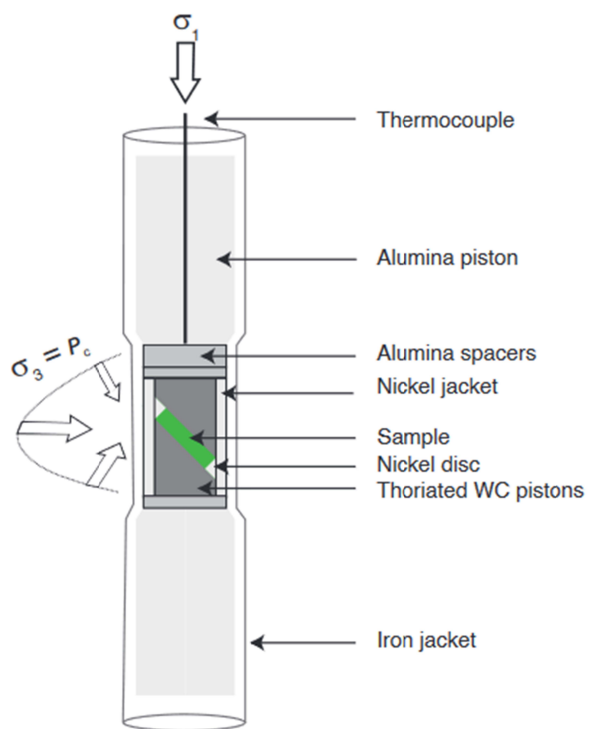
89 The present study investigated the microstructural behavior of several deformed partially  
90 molten aggregates. The sample-scale behavior of one set of samples was previously reported in  
91 Zimmerman et al. (1999). In addition, the behavior of two additional samples deformed at higher  
92 stress conditions was examined. We characterize the co-evolution of melt preferred orientation  
93 (MPO) of the liquid network and crystallographic and shape preferred orientations (CPOs and  
94 SPOs) of the solid phase, from which we infer the influence of stress and strain on CPO, SPO  
95 and MPO development in the deformed samples. We then use our experimental results to  
96 calculate predicted seismic anisotropy in these samples, and discuss the relative importance of  
97 melt and crystalline orientations on seismic anisotropy in samples deformed to small strains.

98

## 99 **2. Methods**

### 100 *2.1 Experimental deformation and imaging details*

101 Samples of olivine  $\pm$  orthopyroxene and 2-4 wt% mid-ocean ridge basalt (MORB) were  
102 created by hot pressing cold-pressed powders in a gas-medium deformation apparatus (Paterson,  
103 1990) at 1250°C at 300 MPa for  $\sim$ 3 hours. Samples were then cored and sliced from the hot-  
104 pressed cylinders and placed between thoriated tungsten pistons pre-cut at a 45° angle, as  
105 illustrated in Figure 1. These samples were subsequently deformed at the University of  
106 Minnesota in the gas-medium deformation apparatus at 1250°C and 300 MPa confining pressure.  
107 Under strain rates of  $10^{-4}$ - $10^{-6}$  s $^{-1}$ , samples reached shear stresses of  $\tau = 50$ -175 MPa and strains  
108 of  $\gamma = 0.32$ -2.3. After deformation, samples were cut perpendicular to the shear plane and  
109 parallel to the shear direction, as indicated in Figure 2. A Zeiss Merlin scanning electron  
110 microscope (SEM) in the MIT Materials Research Laboratory was used to create backscattered  
111 electron (BSE) images at 15 – 20 kV accelerating voltage of these 2-D flat sections. In addition  
112 electron backscattered diffraction (EBSD) maps and energy dispersive spectra (EDS) maps were  
113 collected using a Camscan X500FE CrystalProbe at the Université Montpellier 2 at an  
114 acceleration voltage of 20 kV and a step size of 0.2 – 0.6  $\mu$ m.

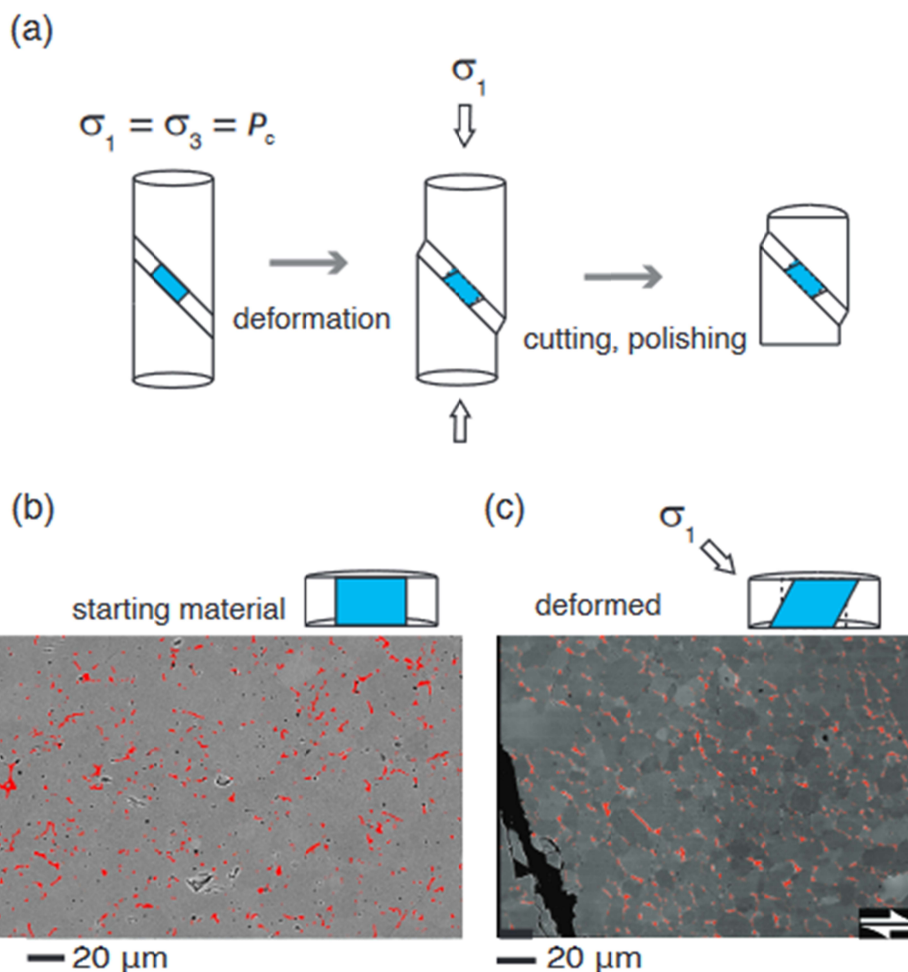


115

116

117

Figure 1: Schematic drawing of the sample setup for deformation experiments.



118  
 119 Figure 2: Sample preparation after deformation and orientation of cuts. (a) Experimental  
 120 work flow for deformation and creation of 2-D sections. SEM images of orientation and  
 121 appearance of the olivine-melt aggregates (b) prior to and (c) after deformation, with melt  
 122 highlighted in red.

123

## 124 2.2 Quantitative image analysis methods

125 We used the projection-based method PAROR (Heilbronner and Barrett, 2014, Chapter  
 126 14) to analyze the grain-scale MPOs and SPOs. This method yields the direction of the longest  
 127 and shortest projections of particle elements. In contrast to the more common ellipse-fitting  
 128 method of determining short and long axes, PAROR does not require the shortest and longest  
 129 directions to be perpendicular to each other and is therefore well suited for analyzing shapes of

130 irregular objects such as melt pockets. The shape preferred orientation,  $\alpha_p$ , is calculated relative  
 131 to the shortest projection direction  $\alpha_{\min}$  such that

132

$$133 \quad \alpha_p = 90^\circ - \alpha_{\min} . \quad (1)$$

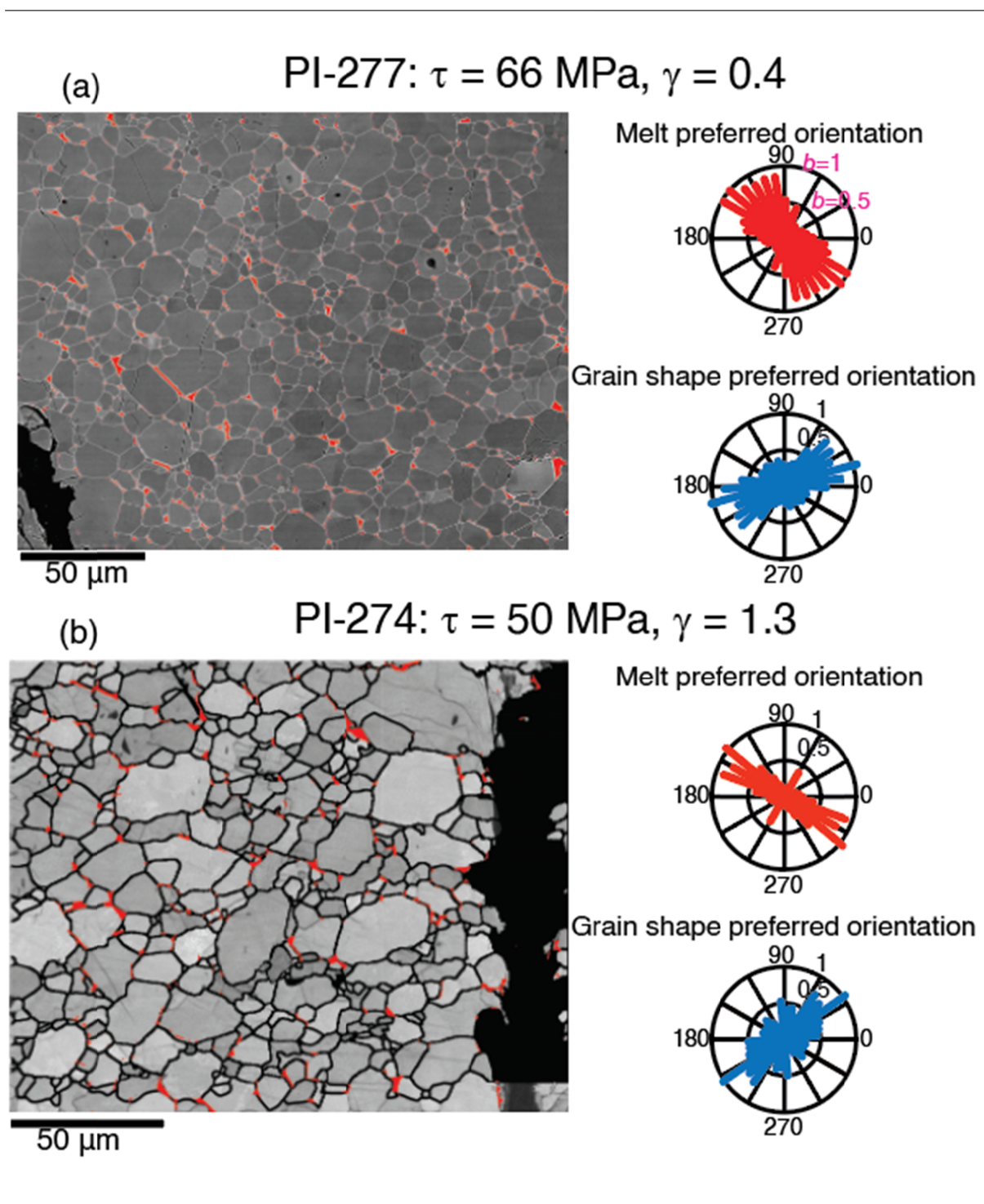
134

135 Note that values of  $\alpha_p$  are symmetric around  $180^\circ$ , so that for  $\alpha_{\min} > 90^\circ$ , negative values  
 136 are converted to their positive conjugate (i.e.,  $-30^\circ$  is the same as  $150^\circ$ ). We described the  
 137 orientations of grains and melt pockets using an orientation distribution function (ODF)  
 138 visualized as rose diagrams, normalized such that the longest axis is 1 and the shortest axis is  
 139 reported as a percentage relative to the longest axis, as illustrated in Figure 3.

140 The strength of the preferred orientation is quantified by its bulk aspect ratio,  $b/a$ , a  
 141 comparison of the longest,  $a$ , and the shortest,  $b$ , projections of all the analyzed melt pockets. A  
 142 high value of the  $b/a$  ratio indicates that little difference exists between the shortest and longest  
 143 axes, and hence the shape is close to isotropic. In contrast, a lower value of  $b/a$  indicates a  
 144 stronger preferred orientation. We also calculated the size of segmented objects as an equivalent  
 145 area circle with diameter  $d_{equ}$ . Because both melt pocket size and grain size distributions  
 146 frequently follow a log-normal distribution, we report the mode of the log-normal probability  
 147 distribution as the most common size for melt pockets or grains in a given sample.

148 We analyzed the orientation of a sample-scale melt network with the autocorrelation  
 149 function (ACF; Heilbronner and Barrett, 2014, Chapter 20). The autocorrelation function  
 150 quantifies the orientation and spatial frequency of the patterns in an image without the  
 151 segmentation of individual features. This approach is therefore well suited for analyzing large-  
 152 scale, fine-feature patterns. Angles are measured counter-clockwise from  $0^\circ$  (east) to  $180^\circ$   
 153 throughout this manuscript.

154



155  
 156 Figure 3: 2-D maps of two samples, one deformed to (a) low strain and the other to (b)  
 157 high strain. The grains are outlined and melt pockets are highlighted in red overlaying SEM  
 158 images of the samples. The melt and grain preferred orientations obtained from these images are  
 159 represented as rose diagrams in red and blue, respectively.

160

161 

### 2.3 *Melt network image analysis*

162 Melt pockets, which are 2-D cross-sections through a 3-D melt network, were analyzed at  
163 the grain scale and at the sample scale. To measure grain-scale MPO, individual pockets were  
164 traced from EDS and band-contrast images such as those in Figure 3, Figure 4a, and 4b. These  
165 traced images were then thresholded to binary, black and white images for segmentation. Only  
166 pockets above a minimum size of 10 pixels (at pixel resolutions of 0.02 – 0.4  $\mu\text{m}$ ) were analyzed  
167 so as to avoid effects from poorly defined small melt pockets. We quantified the MPO and  
168 strength of alignment in a sample based on two factors, orientation ( $\alpha_p$ ) and bulk aspect ratio  
169 ( $b/a$ ), as described above.

170 To identify larger-scale melt patterns, we used EDS composition maps of calcium, an  
171 element not present in significant concentration in olivine, as a tracer for melt. We segmented  
172 these maps to create binary images of individual melt pockets, which we analyzed using the ACF  
173 over the entire sample imaged.

174

175 

### 2.4 *Grain-shape preferred orientation and crystallographic preferred orientation analyses*

176 The shape preferred orientation was obtained from manual tracing of grains on SEM  
177 maps of the 2-D slices, as well as from EBSD data. We characterize the shape preferred  
178 orientation of the grains in the same manner as the grain-scale MPO described above.  
179 Representative data are displayed in Figure 3.

180 EBSD data were collected at two scales, analogous to the melt network analyses. A low-  
181 resolution map (0.6- $\mu\text{m}$  step size) covered large parts of the whole sample, and a high-resolution  
182 map (0.2- $\mu\text{m}$  step size) focused on the intracrystalline deformation features, highlighted in  
183 Figures 4c-d. The EBSD data were then analyzed using the MTEX toolbox (<https://mtextoolbox.github.io/>) to characterize the 3-D orientation of the crystallographic axes. The  
184 crystallographic preferred orientation is defined by an ODF describing the direction of the three  
185 mutually perpendicular crystallographic axes in the olivine crystals in each sample. This ODF is  
186 represented graphically as a pole figure depicting multiples of uniform density (M.U.D.) in an  
187 equal-area, upper hemisphere projection, indicating areas of high and low concentrations of each  
188 of the three crystallographic axes of olivine, as indicated in Figures 4e-f. We also collected the  
189 misorientations of the subgrains in the high-resolution EBSD maps, defined by the difference in  
190

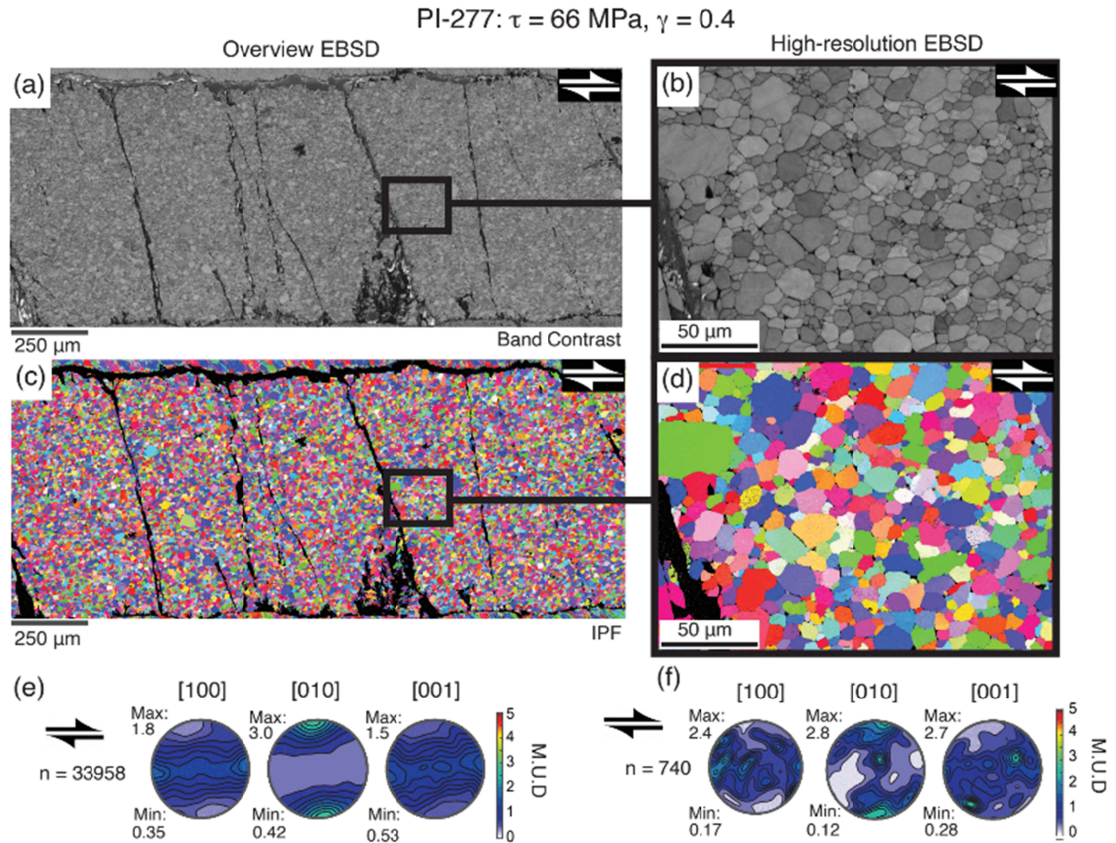
191 internal pixel orientations from the mean orientation of an entire grain, which allowed us to  
192 examine internal deformation of grains.

193

#### 194 *2.5 Calculation of seismic anisotropy*

195 To constrain the microstructural contributions of MPO and CPO to the generation of  
196 seismic anisotropy in olivine-melt aggregates, we followed the Gassman poroelastic differential  
197 effective medium method as applied in a Matlab model, GassDEM (Kim et al., 2019). This  
198 method uses the Voigt elastic tensor calculated from the CPO, then treats melt inclusions as an  
199 oriented fluid-filled crack.

200 We modeled melt pockets as penny-shaped ellipsoids, in which the  $a:b:c$  axes of the  
201 shape followed the ratio  $1:b:1$ , where  $b$  is the shortest projection length of the melt pocket  
202 normalized by the longest projection length (equivalent to the  $b/a$  reported for all MPOs), and  
203 using the orientations of our MPOs such that the azimuth of an inclusion is the angle at which  $b$   
204 is oriented with  $0^\circ = E$  and  $90^\circ = N$ . These orientations were rotated during input into the  
205 GassDEM interface, which takes  $0^\circ = N$  and  $90^\circ = W$ . We took the high-frequency elastic  
206 constants of the resultant tensor calculated with 2.5 wt% melt.



207  
 208 Figure 4: (a), (b) Band contrast images and (c), (d) orientation maps for sample PI-277.  
 209 Pole figures are equal-area projections scaled as multiples of uniform distribution (M.U.D.). (e)  
 210 Overview EBSD pole figures correspond to a larger number of crystals, while (f) high-resolution  
 211 EBSD pole figures include a smaller number of crystals in greater detail, resulting in more  
 212 pronounced point maxima.

213

### 214 3. Results

#### 215 3.1 MPO - Melt preferred orientation

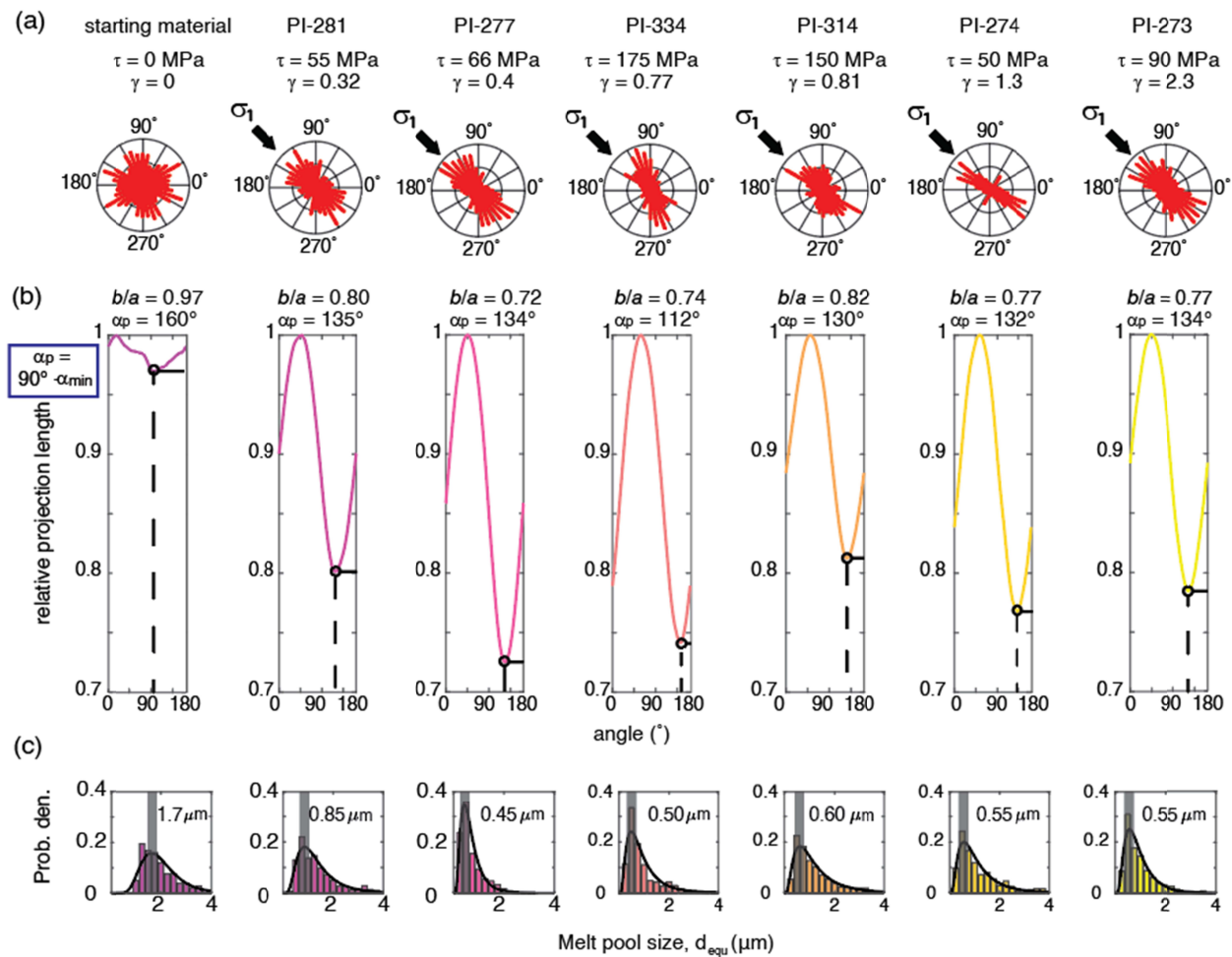
##### 216 3.1.1 Grain-scale melt alignment

217 The individual orientations of grain-scale melt pockets, which were collected for all  
 218 analyzed samples, are summarized in Figure 5. The melt preferred orientation in the starting  
 219 material is very weak, and the  $b/a$  aspect ratio of 0.97 from all aggregated individual melt  
 220 pockets indicates a nearly isotropic shape. The strength of the MPO increased at the onset of  
 221 deformation and was fully established by  $\gamma \approx 0.5$ , with melt pockets oriented close to the  
 222 direction of the maximum applied principal stress at  $135^\circ$ . The MPO at this scale, once

223 established, was essentially independent of further strain; it varied by only  $\pm 5^\circ$  from parallel to  
 224 the loading direction, with one exception, over the entire range of strains and stresses explored.

225 The projection curves from the PAROR orientations in Figure 5b document that the  
 226 strongest alignment, a  $b/a$  ratio of 0.72, formed by a strain of  $\gamma = 0.4$ . At strains of  $\gamma > 0.4$ , melt  
 227 pockets also became slightly more isotropic with increasing strain. Melt pocket sizes also  
 228 converged to a common size at low strains, as in Figure 5c. Starting material melt pocket size  
 229 was  $\sim 2 \mu\text{m}$ , while melt pocket sizes shrank to  $\sim 0.9 \mu\text{m}$  by  $\gamma = 0.4$  and converged to  $d_{\text{equ}} \approx 0.5 \mu\text{m}$   
 230 by  $\gamma > 0.4$  regardless of the magnitude of stress or strain.

231



232

233 Figure 5: Evolution of MPO as a function of strain. (a) Rose diagrams from orientation of  
 234 longest projection axes of each individual melt pocket, with the longest segments indicating the  
 235 most common orientation of the longest projection axes. (b) Projection functions from SURFOR  
 236 with minima (shortest projection axis) and the corresponding preferred orientation labeled. (c)

237 Melt pocket size histograms with log-normal fit overlain. The mode of the distribution is labeled  
238 and indicated with a gray bar.

239

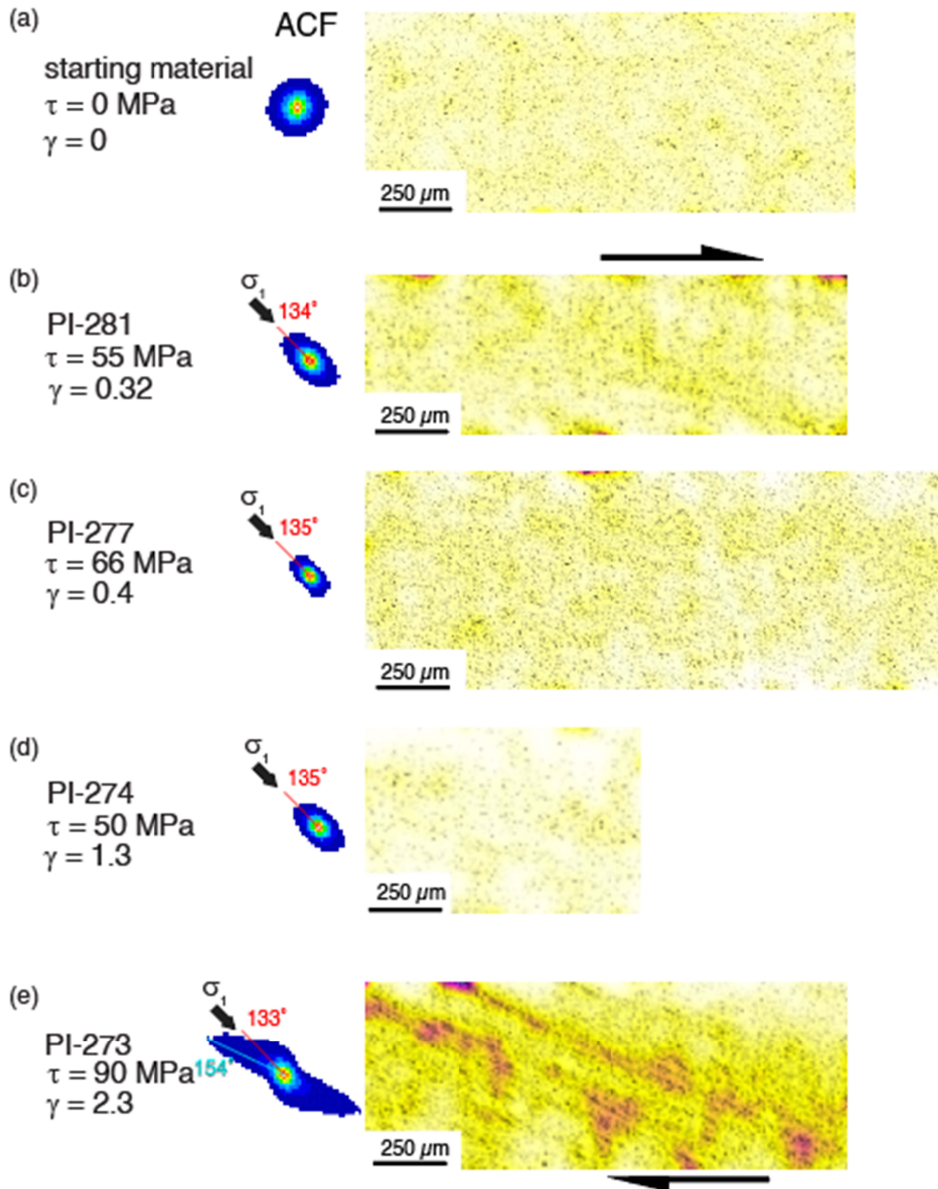
### 240 3.1.2 *Sample-scale melt alignment*

241 The initial orientation and spatial distribution of melt at the sample scale was isotropic, as  
242 revealed by the ACF analyses of the binary images in Figure 7. At low strains, the spatial  
243 distribution of the melt remained isotropic, but the network of melt pockets developed a  
244 preferred orientation parallel to the direction of applied stress at the sample scale, in agreement  
245 with the orientation of melt observed at the grain scale. In the samples deformed to the highest  
246 strain, melt began to segregate into relatively melt-rich and melt-poor regions, and a secondary  
247 orientation at long correlation length scales (i.e., the spatial distance over which a feature can be  
248 correlated with itself) began to form at  $\sim 155^\circ$  ( $\sim 20^\circ$  to  $\sigma_1$ ,  $\sim 25^\circ$  to the shear zone boundary).  
249 Short-correlation length scales (i.e., those close to the origin on the ACF plot) still retained an  
250 orientation sub-parallel to the loading direction.

251

### 252 3.1.3 *Melt alignment summary*

253 Rapid evolution of the MPO occurred in the earliest stages of shearing. A clear MPO  
254 parallel to  $\sigma_1$  was already developed at a strain of  $\gamma \approx 0.3$ . The maximum strength of melt  
255 preferred orientation occurred at a strain of  $\gamma \approx 0.4$ . The MPO thus reached a steady state  
256 orientation and strength after only a relatively small strain increment, a trend that does not  
257 depend on stress within the studied range. The grain-scale MPO from smaller areas described in  
258 Section 3.1.1 has larger variations in orientation than ACF-derived orientations over much larger  
259 areas. At the highest strain explored, incipient segregation into melt-rich and melt-poor domains  
260 led to the development of a secondary preferred orientation at  $25^\circ$  to the shear zone boundary.



261

262 Figure 6: Sample-scale melt network analyzed by the autocorrelation function (ACF).

263 Conditions of our (a) hot-pressed starting material and (b)-(e) four deformation experiments with

264 each corresponding ACF (central column) and binary melt map contoured from low melt density,

265 in white, to high melt density, in purple (rightmost column). The distance from the center of an

266 ACF represents the length scale over which a feature can be correlated (i.e., closer to center of an

267 ACF = shorter-scale feature correlation, while further away from the center of the ACF = longer-

268 scale feature correlation).

269

270 *3.2 Grain shape and crystallographic preferred orientation (SPO & CPO)*

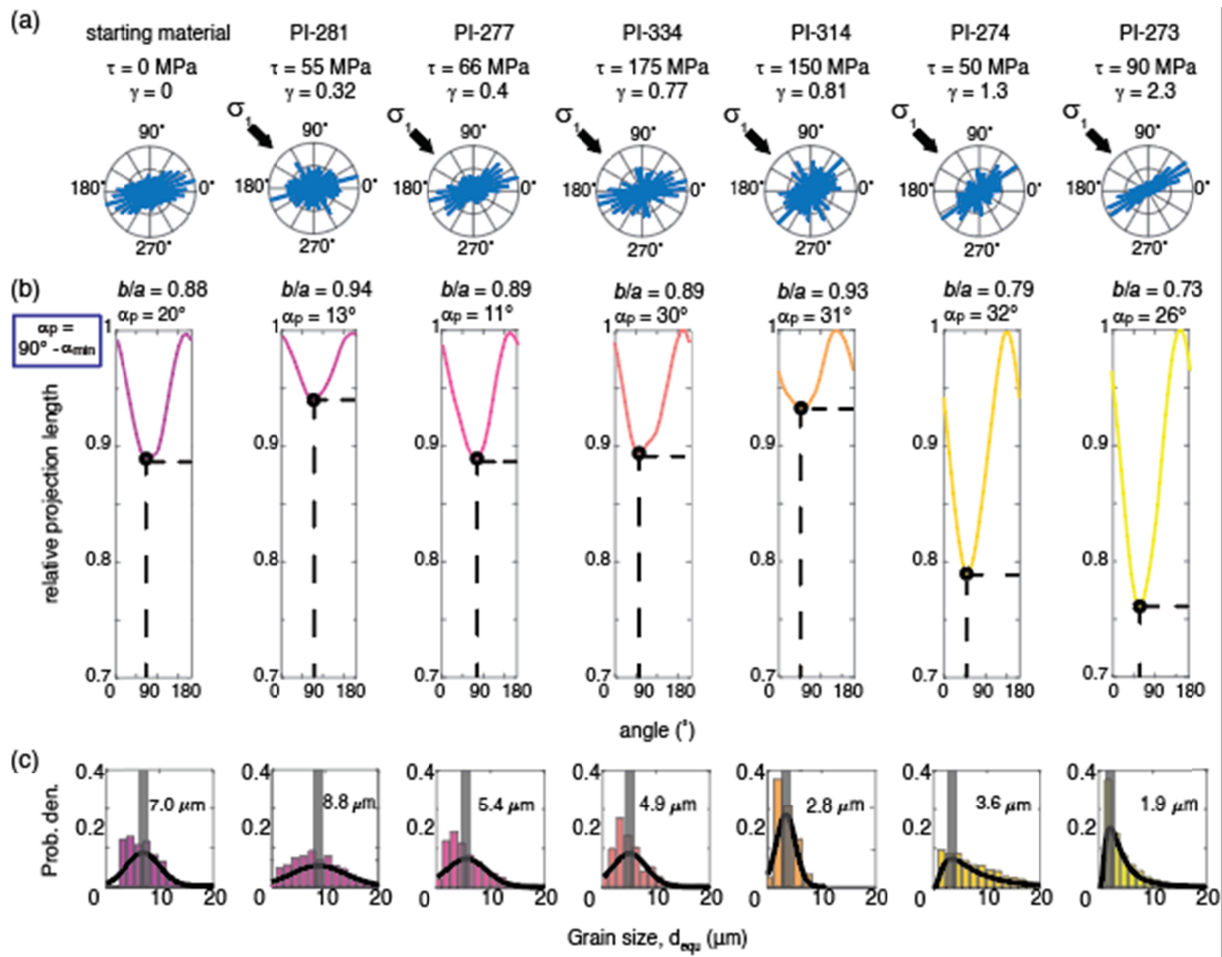
271 3.2.1 SPO - Shape preferred orientation

272 The SPO of all grains was analyzed, and is reported in Figure 7. At low strains, grains  
273 remained oriented approximately perpendicular to the direction of  $\sigma_1$ . This orientation did not  
274 evolve significantly with strain until  $\gamma > 0.8$ , at which point the orientation began to rotate into  
275 the instantaneous stretching direction, becoming closer to perpendicular to the direction of  $\sigma_1$ .

276 The bulk aspect ratios,  $b/a$ , and preferred orientations,  $\alpha_p$ , of the grains (Figure 7b) did  
277 not change in a significant way as strain increases for  $\gamma < 1.3$ . The grain shape aspect ratios  
278 remained close to isotropic (with a minimum of 0.88 at  $\gamma = 0$  and a maximum of 0.94 at  $\gamma = 0.3$ )  
279 for all but the sample deformed to the highest strain. A stronger SPO, indicated by a  $b/a$  of 0.79,  
280 formed by  $\gamma = 1.3$ , as long axes of the deforming grains began to align. This behavior indicates  
281 that the grain shape itself was changing slowly at lower strains but evolved into a stronger  
282 preferred orientation as strain increased to  $0.8 > \gamma > 1.3$ .

283 Grain sizes generally decreased with increasing stress. The distribution of grain sizes in  
284 the starting material (Figure 7c) peaked between 5 and 10  $\mu\text{m}$  after hot-pressing for 3 h. At  $\gamma =$   
285 0.3, grains exhibited a normal distribution curve with a peak at  $\sim 9 \mu\text{m}$ , while all samples  
286 deformed to higher strain had a log-normal distribution curve of grain sizes peaking between 2  
287 and 4  $\mu\text{m}$ . Grain sizes, aspect ratios, and shape fabrics wavered around similar values at very low  
288 strains ( $\gamma < 1.3$ ); at the highest strains examined here, both aspect ratios and grain sizes began to  
289 decrease. SPO thus required higher strains to develop and was less sensitive to the early stages of  
290 deformation than MPO.

291



292

293 Figure 7: Grain SPO evolution as a function of strain. (a) Rose diagrams from orientation  
 294 of longest projection axes of each individual grain. (b) Projection functions with minima  
 295 (shortest projection axis) and the corresponding preferred orientation labeled. (c) Grain size  
 296 distribution, with normal or log-normal fit overlain. The mode of the distribution is labeled and  
 297 indicated with a gray bar.

298

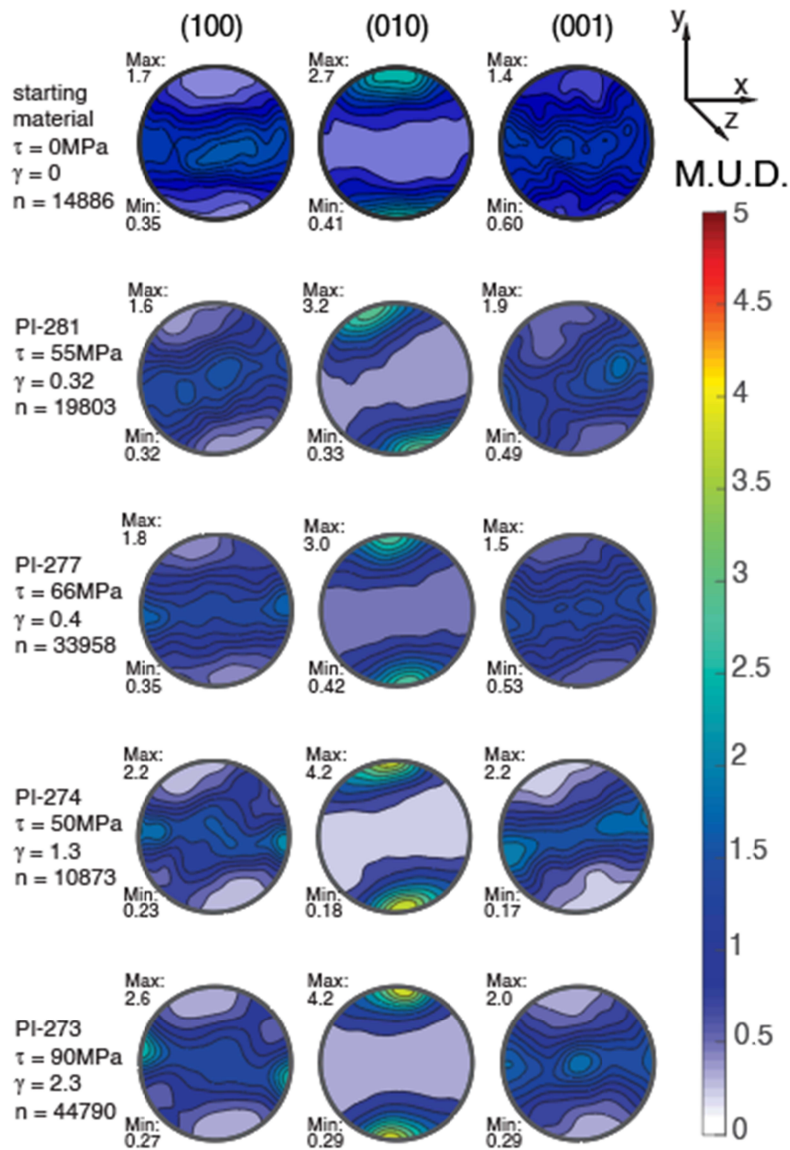
### 299 3.2.2 CPO - Crystallographic preferred orientation

300 The CPOs of deformed samples in Figure 8 evolved with increasing strain. The starting  
 301 material had a well-developed CPO with [010] axes aligned parallel to the long axis of the  
 302 sample and the [100] and [001] axes in weak girdles perpendicular to the long axis of the sample.  
 303 As strain increased, alignment of the [010] axes increased in strength, while the [100] and [001]  
 304 axes remained girdled. At low strains, the orientations rotated antithetically away from the shear

305 plane, such that the [010] axes were 75-90° from the shear plane and the [100] and [001] axes  
306 girdled within 5° of the shear plane. At the highest strain reached in our experiments,  $\gamma = 2.3$ , the  
307 a-girdle rotated nearly parallel to  $\sigma_1$  and developed stronger clustering, while the [001] axes  
308 began to cluster in the center of the pole figure. A secondary maximum orientation of the [100]  
309 axes developed 85-90° to  $\sigma_1$ .

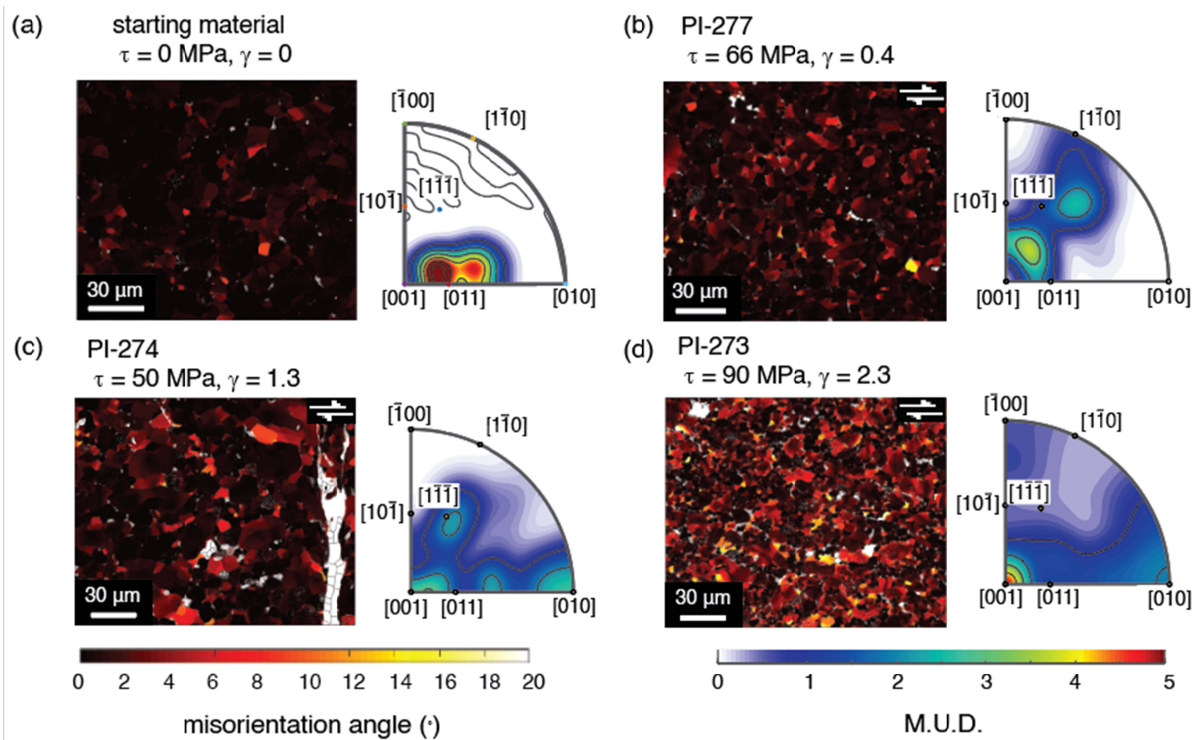
310 The effect of increasing strain on intracrystalline structure is illustrated in Figure 9. As  
311 seen in Figure 9a, subgrains in olivine crystals increased in density and misorientation as strain  
312 increased; the starting material had a low subgrain density and low misorientation angles ( $<10^\circ$ )  
313 within those subgrains, while the sample deformed to  $\gamma = 2.3$  had subgrains with relatively high  
314 misorientations ( $>10^\circ$ ) in nearly every grain. Inverse pole figures of the misorientations  
315 demonstrate that, with increasing strain, rotation around the [001] axis became increasingly  
316 common. The development of a subordinate maximum also suggests rotation around the [010]  
317 axis.

318 Similar to SPOs, CPOs did not change much in the early stages of deformation. The  
319 orientations of the crystallographic axes shifted only slightly, as the [010] planes first rotated  
320 antithetically to the shearing direction and then rotated into the shear plane. At strains of  $\gamma = 1.3 -$   
321 2.3, the [010] planes were rotated slightly synthetical to the imposed shear direction. The  
322 strength of the CPO generally increased as strain increased.



323  
 324 Figure 8: CPO evolution with increasing strain. Minima and maxima are reported as  
 325 multiples of uniform distribution, M.U.D., and  $n$  is the number of grains surveyed in each map.  
 326  
 327

328



329

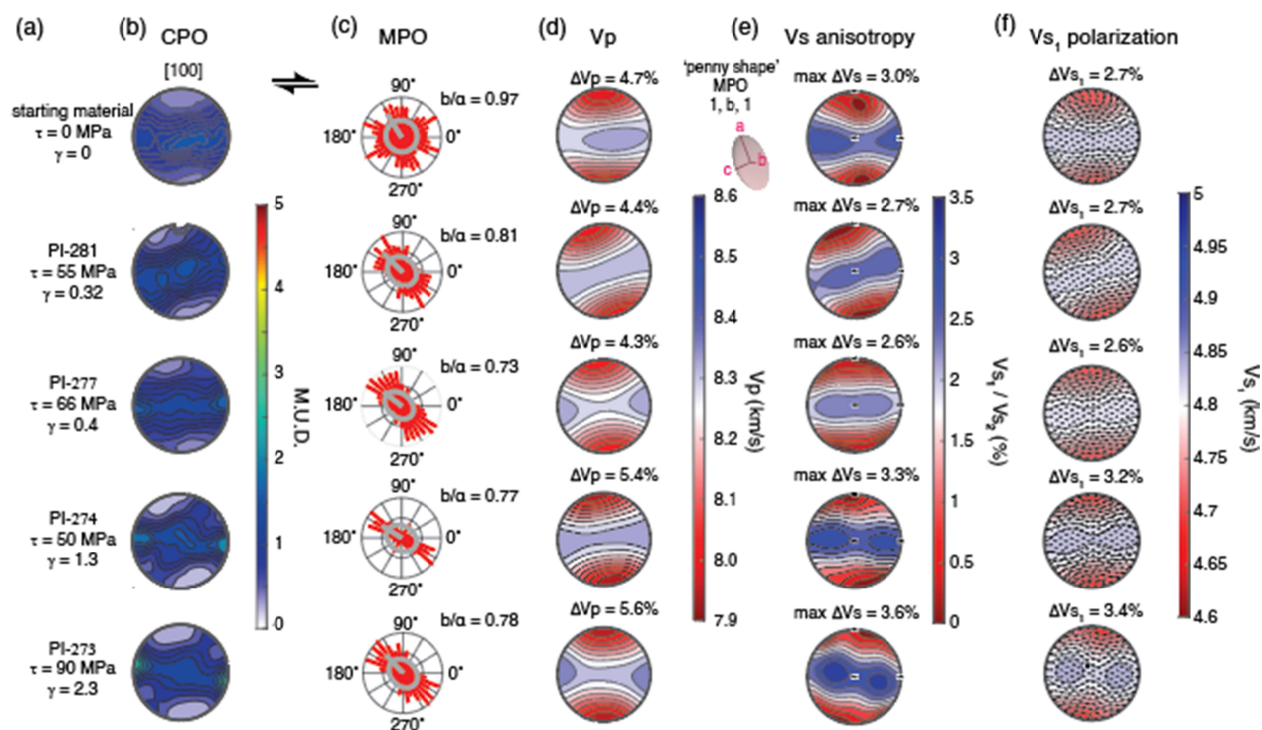
330 Figure 9: Misorientation maps and inverse pole figures of misorientation axes in  
 331 crystallographic reference frame from (a) the starting material, (b) a sample sheared to low  
 332 strain, and (c)-(d) two samples deformed to high strain. All images are shown at the same  
 333 scale.

334

### 335 3.3 Calculation of seismic anisotropy

336 The effective calculated seismic anisotropy of each of our partially molten rocks is  
 337 presented in Figure 10. We express three measures of seismic anisotropy: the % difference in  $V_p$   
 338 wavespeeds, calculated as the difference between fastest and slowest orientations within the  
 339 tensor, the % difference in  $V_s$  wavespeeds, calculated as the greatest difference between  $V_{S1}$  and  
 340  $V_{S2}$  within the tensor, and the  $V_{S1}$  anisotropy, calculated as the greatest difference between  $V_{S1}$   
 341 wavespeeds. The pole figures in Figure 10 show the distribution of  $V_p$  wavespeeds, the  
 342 distribution of the difference between  $V_{S1}$  and  $V_{S2}$  wavespeeds, and the velocity and polarization  
 343 of  $V_{S1}$  waves.

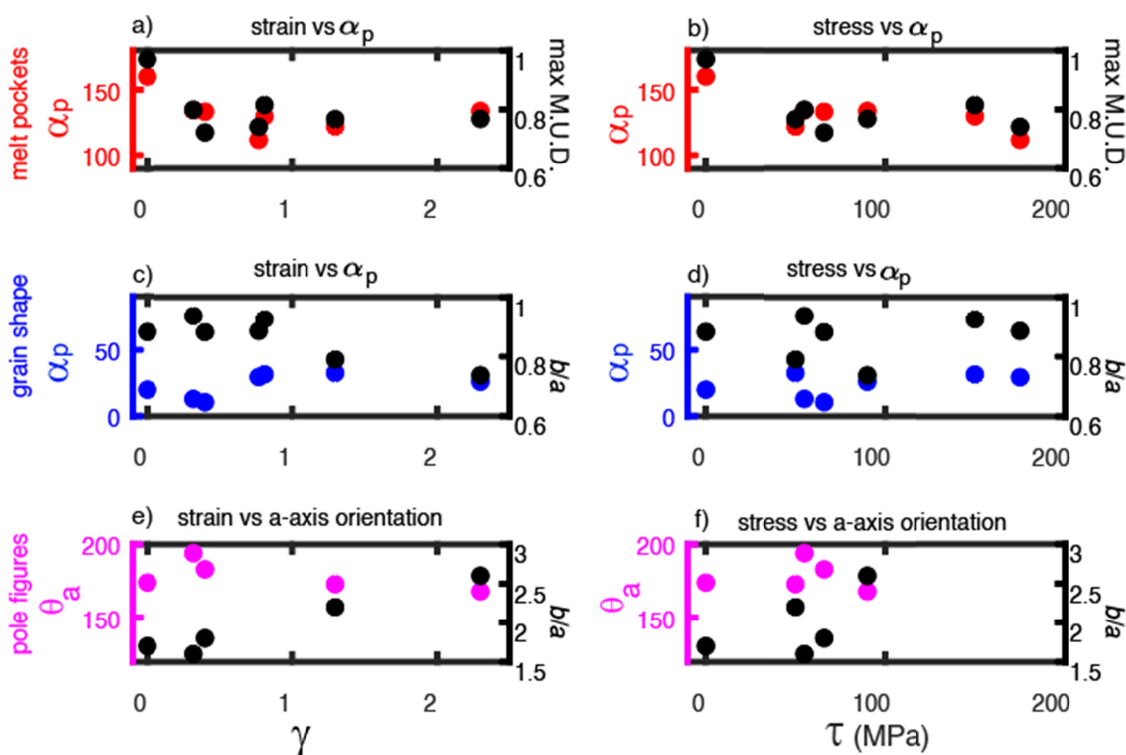
344 At the onset of deformation, the calculated values of the seismic anisotropy  
 345 decreased. However, at  $\gamma \gtrsim 0.4$ , the effective calculated values of seismic anisotropy increased  
 346 with increasing strain. This behavior parallels the development of MPOs and CPOs with  
 347 increasing strain. At low strains, the CPO was weak, and the MPO was oriented antithetical to  
 348 the shearing direction and parallel to  $\sigma_1$ . The  $\sigma_1$ -parallel melt orientation was oblique to the  
 349 orientation of the crystallographic axes, which were aligned in a girdle parallel to the shear  
 350 plane. The anisotropy determined for our lower strain tests reflects a competition between MPO  
 351 and CPO. As a result, the melt decreased the CPO-generated anisotropy with respect to a melt-  
 352 free sample. As strain increased, the strength and direction of the preferred orientation of the  
 353 melt network did not change, but the CPO became stronger and the [100] axes become more  
 354 aligned parallel to the shear plane. At higher strains, the CPO developed a stronger alignment  
 355 and became the dominant determinant of anisotropy. As this change occurred, the seismic  
 356 anisotropy of  $V_p$ ,  $V_s$ , and  $V_{s1}$  all steadily increased.  
 357



358  
 359 Figure 10. Calculated seismic anisotropy from our CPO and MPO data. (a)  
 360 Individual experiment numbers and associated conditions, (b) a-axis orientation pole  
 361 figures, and (c) MPO visualized in the rose diagrams. The mean melt inclusion shape and  
 362 orientation is represented as a gray ellipsoid superimposed on rose diagrams for (d)  $V_p$

363 anisotropy (difference between slowest and fastest p-wave velocity direction), (e)  $V_s$   
 364 anisotropy (difference between orthogonally polarized  $V_{s1}$  and  $V_{s2}$  velocities), and (f)  $V_{s1}$   
 365 polarization and velocity.

366  
 367



368  
 369 Figure 11. Summary of microstructural data. (a)-(d) Preferred orientation angle  
 370 (from  $0^\circ = E$ ) as a function of strain (a), (c) and stress (b), (d) for grain-scale melt pockets  
 371 (a), (b) and grains (c), (d). Preferred orientation is reported as  $\alpha_p$ , and the strength of the  
 372 preferred orientation is indicated by the  $b/a$  aspect ratio of the fabric. (e)-(f) Orientation of  
 373 the girdle formed by olivine [100] axes ( $\theta_a$ ) as a function of strain (e) and stress (f), with  
 374 the strength of the preferred orientation reported as peak multiples of uniform distribution,  
 375 such that a higher M.U.D. represents a higher concentration of axes aligned at this  
 376 orientation. Note that CPO data are not available for the higher stress tests.

377

## 378 4. Discussion

### 379 4.1 MPO formation on grain scale and on sample scale

380 Our results demonstrate that MPOs evolve much more quickly at the onset of shear  
381 deformation than either SPO or CPO of the solid grains as summarized in Figure 11. The grain-  
382 scale MPO reacted to changing conditions nearly instantaneously, and a MPO different than that  
383 of the starting material formed at the onset of deformation ( $0 < \gamma < 0.32$ ). A peak in MPO  
384 strength was reached at a shear strain of 0.4, after which the MPO oscillated around a steady  
385 state value; the orientation remained approximately parallel to the direction of maximum  
386 principal stress, and melt pool sizes conformed to  $\sim 0.5 \mu\text{m}$ , accompanied by a slight increase in  
387 melt pocket aspect ratios (Figure 6).

388 There may be a stress dependence in the alignment of the melt preferred orientation with  
389 respect to the sample-scale stress field. Samples deformed to higher stresses displayed a rotation  
390 of the MPO synthetic with the sense of shear away from the loading direction, which is assumed  
391 to correspond to  $\sigma_1$ . This rotation might reflect a local deflection of the  $\sigma_1$  orientation at the  
392 piston-sample interface. At relatively higher stresses, the effective direction of  $\sigma_1$  rotates up to  
393  $20^\circ$  synthetically to the sense of shear, as has been observed in quartz and feldspar shear  
394 deformation experiments via the development of twinning (Pec & Al Nasser, 2021). As such, the  
395 rotation of the grain-scale melt pocket orientation in higher-stress tests is likely a readjustment to  
396 the local effective stress field, so that the MPO still remains parallel to the direction of local  
397 maximum principal stress.

398 Examination of some of the samples used in this study with lower resolution optical  
399 images (tests PI-277, PI-281, PI-274, and PI-273, as reported in Zimmerman et al., 1999), led to  
400 the conclusion that the MPO is inclined at  $\sim 20^\circ$  to the shear plane, antithetic to the shear  
401 direction (i.e., at  $\sim 25^\circ$  to the loading direction). Likewise, analyses of low-resolution optical  
402 images of samples deformed in coaxial compression indicated that the MPO also formed at an  
403 angle of  $\sim 20^\circ$  to the loading direction (Daines & Kohlstedt, 1997; Kohlstedt & Zimmerman,  
404 1996; Zimmerman et al., 1999). Furthermore, melt-rich “bands” observed in experiments on  
405 samples with a short compaction length commonly form at an inclination of  $15^\circ - 20^\circ$  with  
406 respect to the shear plane (also reported as  $25 - 30^\circ$  from the direction of maximum principal  
407 stress) (Holtzman et al., 2003; King et al., 2010; Kohlstedt & Holtzman, 2009). In contrast, our  
408 high-resolution data suggests that the grain-scale melt pockets in these samples are aligned  
409 parallel to the maximum principal stress. The MPO alignment in our tests is in agreement with  
410 observations from analog materials (Takei, 2005) and is consistent with the MPO needed to

411 produce melt rich “bands” inclined  $15 - 20^\circ$  to the shear plane on sample scale within the  
412 framework of two-phase flow theory with viscous anisotropy (Katz & Takei, 2013; Takei &  
413 Holtzman, 2009c, 2009b, 2009a; Takei & Katz, 2013; Taylor-West & Katz, 2015). Local  
414 variations in melt network orientation do exist, as seen in Figure 6; the orientation of larger melt  
415 pockets, perhaps as an aggregation of several smaller pockets, can produce local sub-maxima in  
416 orientation close to  $20^\circ$  for higher-strain samples in which incipient melt segregation is observed.

417 It appears that the scale of observation and the method of analysis (projection-based  
418 methods and autocorrelation-based methods vs. ellipse-fitting methods) may influence estimates  
419 of melt orientation. We propose that individual melt pockets at the grain scale align subparallel  
420 to  $\sigma_1$ , while aggregate melt pockets on the sample scale form an en echelon pattern aligned at a  
421 lower observed angle with respect to  $\sigma_1$  (Figure 6).

422 However, this sample-scale alignment at  $\sim 20^\circ$  with respect to  $\sigma_1$  only occurred in our  
423 highest-strain sample; sample-scale alignment developed parallel to the direction of  $\sigma_1$  in all  
424 other samples. Melt in the highest strain sample also began to segregate into melt-rich and melt-  
425 poor domains, as is typically observed in sheared samples with a short compaction length at  
426 strains of  $\gamma \geq 1$  (King et al., 2010; Kohlstedt & Holtzman, 2009). The emergence of these  
427 “bands” may be the result of viscous anisotropy induced by grain-scale alignment of melt  
428 parallel to  $\sigma_1$  ( $45^\circ$  to the shear plane) and decreasing compaction length as grains recrystallize to  
429 a smaller grain size, documented in Figure 7c. These observations again agree with predictions  
430 from the viscous anisotropy theory framework (Katz & Takei, 2013; Quintanilla-Terminel et al.,  
431 2019; Takei & Holtzman, 2009c; Taylor-West & Katz, 2015), and explain the discrepancy  
432 between experimentally obtained value of  $25^\circ$  for melt orientation and computationally predicted  
433 sub-parallel orientation with respect to  $\sigma_1$ ; both are correct, just at different observation scales.  
434 The closer the sample size or observation scale is to the compaction length, the more likely melt  
435 is to be oriented at  $20^\circ$  to the shear plane; smaller scale melt networks are oriented parallel to  $\sigma_1$ .

436

#### 437 *4.2 Grain SPO and CPO formation*

438 SPO and CPO form much more slowly than MPO. Grains in the starting material had a  
439 SPO and a CPO that developed during hot pressing of the starting material. Individual olivine  
440 grains tend to be elongated along the [100] and [001] axes with the longest straight grain  
441 boundaries lying in the [010] plane (Miyazaki et al., 2013; Qi et al., 2018). Axial compression of

442 these elongated crystals aligns the long axes of the SPO in a girdle perpendicular to the loading  
443 direction. This process produces a SPO-induced CPO, characterized by girdles in [100] and  
444 [001] axes oriented perpendicular to the loading direction and clusters in poles of [010] planes  
445 parallel to the loading direction, as seen in Figure 8. At low strains ( $0.3 < \gamma < 0.8$ ), almost no  
446 change occurred in the size, orientation, and shape fabric of the grains. The SPO began to define  
447 a weak foliation sub-perpendicular to the loading direction at higher strains ( $\gamma > 0.8$ ). The  
448 strength of CPO alignment steadily increased with increasing strain in our experiments,  
449 consistent with numerical models (Boneh et al., 2015) and other experimental results (Boneh &  
450 Skemer, 2014; Hansen et al., 2014; Qi et al., 2018). Although the alignment strength increased,  
451 the evolution of grain size and shape fabric still did not depend systematically on strain or stress  
452 at low strains. The pole figure geometry also did not change significantly until a strain of  $\gamma > 2$ .

453 The CPO of these deformed samples, in which the [010] planes align parallel with the  
454 shear direction and the [100] and [001] axis form girdles parallel to the shearing direction, is one  
455 commonly observed in sheared aggregates of melt-bearing olivine. This CPO may develop if  
456 grains preferentially grow along the [001] direction and then align under the imposed kinematic  
457 boundary conditions; the relative fabric strength thus reflects competition between SPO-induced  
458 and dislocation-induced CPOs (Qi et al., 2018). Misorientation axes (Figure 10) are also  
459 dominantly aligned with [001] with a subordinate maxima around the [010] crystallographic  
460 direction, indicating that (010)[100] is the dominant slip system in our rocks, provided that the  
461 subgrain walls have a tilt character (Prior et al., 2002) as commonly observed in partially molten  
462 olivine rocks (Qi et al., 2018).

463 The observed CPOs could form by passive rotation of grains with a SPO, or by rotation  
464 of individual crystallographic planes due to dislocation motion during deformation.  
465 Intracrystalline misorientation maps displayed in Figure 9 confirm that indeed crystalline grains  
466 are strongly bent. Geometry of pole figure patterns especially in highest strain samples are  
467 similar to an A-type fabric indicative of the easy slip system (010)[100] accommodating  
468 deformation in the shear plane (Karato et al., 2008; Zhang & Karato, 1995). The CPO-generating  
469 mechanisms (SPO-induced CPO and dislocation-induced CPO) are likely competing at low  
470 strains; at higher strains, the more prominent cluster in [100] axes alignment in the shear  
471 direction, together with large intragranular misorientations, indicate that dislocation glide is  
472 dominant in formation of the CPO.

473 It is interesting to note that in the highest-strain experiments, a secondary cluster in [100]  
474 axes orientations forms. This secondary maximum is relatively common in A-type fabrics, but  
475 not well understood. Although Zhang et al. (2000) explained this secondary maximum as a  
476 signature of non-recrystallized grains in a matrix otherwise undergoing dynamic  
477 recrystallization, the grains with this orientation in our sample do not have substantially different  
478 misorientations from the bulk sample. They do, however, have a flatter and weaker SPO than all  
479 other grains in the sample. More work is necessary to understand the processes governing the  
480 formation of this secondary maximum.

481

#### 482 *4.3 Contributions to seismic anisotropy*

483 Measurements of seismic anisotropy in the Earth's lower lithosphere are traditionally  
484 understood to result from a CPO, such that seismologists can use the anisotropy measurements to  
485 infer the direction of flow in the mantle (Long & Becker, 2010). Any change to the CPO in a  
486 given region complicates the interpretation of seismic anisotropy. The presence of melt  
487 introduces further difficulties, as MPO will affect the CPO-induced anisotropy. To robustly  
488 interpret seismic data, it is important to understand relationships between the kinematic boundary  
489 conditions and physical mechanisms involved in creating CPO and MPO in partially molten  
490 rocks.

491 Here, we documented that the CPO alignment strengthens, but does not change much in  
492 orientation in samples sheared to strains of  $\gamma \lesssim 2.5$ . In contrast, the grain-scale melt network  
493 develops a strong preferred orientation parallel to  $\sigma_1$  at the onset of deformation, and this  
494 orientation persists with increasing strain. The strength of the melt alignment saturates at low  
495 strains and does not increase with increasing strain or stress, as can be observed in Figure 5.

496 It follows that at the onset of deformation, the effect of the melt network orientation on  
497 seismic anisotropy is pronounced. The presence of aligned melt alone reduced seismic  
498 wavespeeds and influenced seismic anisotropies, but the relative alignments of the MPO and  
499 CPO determined the extent and magnitude of this change. Because waves are fastest in olivine  
500 along the [100] axes and fastest in partially molten material parallel to the direction of the  
501 alignment of melt, seismic anisotropy is highest when the [100] axes and the MPO are in a  
502 similar orientation. Seismic velocities and anisotropies both decrease at the onset of MPO  
503 formation, if the fast crystalline [100] axes are oriented obliquely to the melt preferred

504 orientation. However, seismic anisotropy increases above  $\gamma \approx 0.8$ , because the CPO strengthens  
505 and the MPO remains unchanged as we demonstrate in Figures 10 and 11.

506 Previous studies of seismic anisotropy caused by an aligned melt network in a rock with  
507 an isotropic CPO determined the strength of anisotropy caused purely by melt orientation (Lee et  
508 al., 2017). In a series of tests with the GassDEM model that covered a range of hypothetical  
509 MPOs and crystalline fabrics, we found that the interplay of MPO and CPO is crucial to  
510 modeling actual seismic anisotropies. As the MPO and the [100] axes of the CPO approach  
511 alignment with increasing strain, anisotropy increases; if these two orientations are not aligned,  
512 as is the case in the initial stages of deformation, the anisotropy decreases relative to that of the  
513 undeformed material. The magnitude of this effect depends on melt fraction as well, such that the  
514 effect of co-aligned MPOs and CPOs increases with increasing melt fraction, while the decrease  
515 in anisotropy due to competing MPO and CPO did not depend significantly on melt fraction.  
516 Anisotropies in  $V_p$  wavespeeds, relative travel times of  $V_s$  waves, and  $V_{s1}$  wavespeeds all  
517 followed the trend described here, but the  $V_{s1}$  anisotropy is particularly sensitive to the effect of  
518 melt fraction. The addition of isotropic (equiaxial) melt reduces seismic velocities and CPO-  
519 induced anisotropies but does not interact with the CPO, and so its effect is less pronounced than  
520 that of oriented melt.

521 Our results demonstrate that CPOs and MPOs evolve over distinct characteristic time-  
522 scales, complicating the interpretation of observed seismic anisotropy in terms of oriented mantle  
523 flow. This conclusion agrees well with studies of fast-deforming zones in Eastern Africa which  
524 suggest that melt alignment contributes noticeably to seismic anisotropy in the shallow upper  
525 mantle (Bastow et al., 2010; Chambers et al., 2021; Hammond, 2014; Kendall et al., 2005). At  
526 greater depths in the mantle where high pressure inhibits partial melting, the CPO is the  
527 dominant mechanism for decoding seismic anisotropy and understanding the direction of mantle  
528 flow.

529 The almost instantaneous development of MPO under differential stress also means that  
530 MPO is a more reliable indicator of instantaneous changes in stress than the CPO is. An abrupt  
531 shift to the local stress field, such as that caused by an earthquake or volcanic eruption, may be  
532 visible in seismic signals as a nearly immediate change in the local seismic anisotropy, as MPOs  
533 forming due to changing stress will compete with established, steady-state CPOs. This behavior

534 may be useful for observing results of changes within the Earth, or for understanding melt  
535 distribution in rapidly evolving planetary settings dominated by orbital tidal stresses.

536

## 537 **5. Conclusions**

538 We found that as a partially molten olivine-basalt aggregate deforms:

- 539 • Grain-scale melt alignment forms parallel to  $\sigma_1$  at the onset of deformation ( $0 < \gamma$   
540  $< 0.3$ ) and persists to the highest strains studied here. Strain does not affect the  
541 orientation or strength of this grain-scale melt alignment.
- 542 • A distinct sample-scale melt preferred orientation forms  $20^\circ$  oblique to  $\sigma_1$  at  
543 higher strain due to an echelon arrangement of grain-scale melt pockets and  
544 incipient melt segregation.
- 545 • Samples develop a CPO during hot pressing and the pole figure geometry doesn't  
546 change significantly over all explored conditions. The strength of the alignment  
547 increases steadily with increasing strain.
- 548 • SPOs produced during hot-pressing randomize at low to intermediate strains  $0.3 >$   
549  $\gamma < 1.3$  and eventually develop a moderately strong SPO oriented at  $\sim 30^\circ$  to the  
550 shear plane at high strain ( $\gamma > 1.3$ ).
- 551 • Melt preferred orientation is established more quickly in response to changes in  
552 the stress field than crystallographic preferred orientation or grain shape preferred  
553 orientation. The MPO is thus more reactive to changing stress conditions than the  
554 CPO.
- 555 • As deformation progresses and strain increases, the grain-scale MPO does not  
556 change, but the sample-scale melt network coalesces into bands with a secondary  
557 orientation. At these higher strains, a dislocation-induced CPO forms and  
558 strengthens and hence CPO contributes more to seismic anisotropy than MPO  
559 does at high strains.
- 560 • At small strains or over short observable timescales, the MPO may thus be more  
561 visible than the CPO in changes to seismic anisotropy, providing insight into the  
562 stress field orientation in quickly deforming regions of the Earth's upper mantle in  
563 ways that CPO-driven anisotropy cannot.

564

## 565 Acknowledgments:

566 We thank Benjamin Holtzman for commentary and discussion in earlier stages of this project,  
567 Rüdiger Kilian for support with MTEX, and Fabrice Barou for providing EBSD maps. David  
568 Mainprice for connecting us with Eunyoung Kim who provided support with GassDEM. This  
569 work was supported by NSF-EAR 1753482 and NASA-SSW-80NSSC20K0465, with laboratory  
570 technician support funded by NSF-EAR 2054414. C.S. also received support from the MIT  
571 MathWorks Science Fellowship.  
572

## 573 Data availability:

574 Melt maps, EBSD, and analyzed bulk MPO/SPO data are available at  
575 [10.5281/zenodo.7647271](https://doi.org/10.5281/zenodo.7647271).  
576

577  
578 References:

- 579
- 580 Almquist, B. S. G., & Mainprice, D. (2017). Seismic properties and anisotropy of the continental crust:  
581 Predictions based on mineral texture and rock microstructure. *Reviews of Geophysics*, *55*(2),  
582 367–433. <https://doi.org/10.1002/2016RG000552>
- 583 Bastow, I. D., Pilidou, S., Kendall, J.-M., & Stuart, G. W. (2010). Melt-induced seismic anisotropy and  
584 magma assisted rifting in Ethiopia: Evidence from surface waves. *Geochemistry, Geophysics,*  
585 *Geosystems*, *11*(6). <https://doi.org/10.1029/2010GC003036>
- 586 Blackman, D. K., & Kendall, J.-M. (1997). Sensitivity of teleseismic body waves to mineral texture and  
587 melt in the mantle beneath a mid-ocean ridge. *Philosophical Transactions of the Royal Society of*  
588 *London. Series A: Mathematical, Physical and Engineering Sciences*, *355*(1723), 217–231.
- 589 Boneh, Y., Morales, L. F. G., Kaminski, E., & Skemer, P. (2015). Modeling olivine CPO evolution with  
590 complex deformation histories: Implications for the interpretation of seismic anisotropy in the  
591 mantle. *Geochemistry, Geophysics, Geosystems*, *16*(10), 3436–3455.  
592 <https://doi.org/10.1002/2015GC005964>

- 593 Boneh, Y., & Skemer, P. (2014). The effect of deformation history on the evolution of olivine CPO. *Earth*  
594 *and Planetary Science Letters*, 406, 213–222. <https://doi.org/10.1016/j.epsl.2014.09.018>
- 595 Chambers, E. L., Harmon, N., Rychert, C. A., & Keir, D. (2021). Variations in melt emplacement beneath  
596 the northern East African Rift from radial anisotropy. *Earth and Planetary Science Letters*, 573,  
597 117150. <https://doi.org/10.1016/j.epsl.2021.117150>
- 598 Daines, M. J., & Kohlstedt, D. L. (1997). Influence of deformation on melt topology in peridotites. *Journal*  
599 *of Geophysical Research: Solid Earth*, 102(B5), 10257–10271.  
600 <https://doi.org/10.1029/97JB00393>
- 601 Hammond, J. O. S. (2014). Constraining melt geometries beneath the Afar Depression, Ethiopia from  
602 teleseismic receiver functions: The anisotropic H-κ stacking technique. *Geochemistry,*  
603 *Geophysics, Geosystems*, 15(4), 1316–1332. <https://doi.org/10.1002/2013GC005186>
- 604 Hansen, L. N., Faccenda, M., & Warren, J. M. (2021). A review of mechanisms generating seismic  
605 anisotropy in the upper mantle. *Physics of the Earth and Planetary Interiors*, 313, 106662.  
606 <https://doi.org/10.1016/j.pepi.2021.106662>
- 607 Hansen, L. N., Zhao, Y.-H., Zimmerman, M. E., & Kohlstedt, D. L. (2014). Protracted fabric evolution in  
608 olivine: Implications for the relationship among strain, crystallographic fabric, and seismic  
609 anisotropy. *Earth and Planetary Science Letters*, 387, 157–168.  
610 <https://doi.org/10.1016/j.epsl.2013.11.009>
- 611 Heilbronner, R., & Barrett, S. (2014). *Image Analysis in Earth Sciences: Microstructures and Textures of*  
612 *Earth Materials*. Springer-Verlag. <https://doi.org/10.1007/978-3-642-10343-8>
- 613 Hier-Majumder, S. (2011). Development of anisotropic mobility during two-phase flow. *Geophysical*  
614 *Journal International*, 186(1), 59–68. <https://doi.org/10.1111/j.1365-246X.2011.05024.x>

- 615 Holtzman, B. K., Groebner, N. J., Zimmerman, M. E., Ginsberg, S. B., & Kohlstedt, D. L. (2003). Stress-  
616 driven melt segregation in partially molten rocks. *Geochemistry, Geophysics, Geosystems*, 4(5).  
617 <https://doi.org/10.1029/2001GC000258>
- 618 Holtzman, B. K., & Kendall, J.-M. (2010). Organized melt, seismic anisotropy, and plate boundary  
619 lubrication. *Geochemistry, Geophysics, Geosystems*, 11(12).  
620 <https://doi.org/10.1029/2010GC003296>
- 621 Karato, S., Jung, H., Katayama, I., & Skemer, P. (2008). Geodynamic Significance of Seismic Anisotropy of  
622 the Upper Mantle: New Insights from Laboratory Studies. *Annual Review of Earth and Planetary  
623 Sciences*, 36(1), 59–95. <https://doi.org/10.1146/annurev.earth.36.031207.124120>
- 624 Katz, R. F., & Takei, Y. (2013). Consequences of viscous anisotropy in a deforming, two-phase aggregate.  
625 Part 2. Numerical solutions of the full equations. *Journal of Fluid Mechanics*, 734, 456–485.  
626 <https://doi.org/10.1017/jfm.2013.483>
- 627 Kendall, J.-M., Stuart, G. W., Ebinger, C. J., Bastow, I. D., & Keir, D. (2005). Magma-assisted rifting in  
628 Ethiopia. *Nature*, 433(7022), Article 7022. <https://doi.org/10.1038/nature03161>
- 629 Kim, E., Kim, Y., & Mainprice, D. (2019). GassDem: A MATLAB program for modeling the anisotropic  
630 seismic properties of porous medium using differential effective medium theory and  
631 Gassmann's poroelastic relationship. *Computers & Geosciences*, 126, 131–141.  
632 <https://doi.org/10.1016/j.cageo.2019.02.008>
- 633 King, D. S. H., Zimmerman, M. E., & Kohlstedt, D. L. (2010). Stress-driven Melt Segregation in Partially  
634 Molten Olivine-rich Rocks Deformed in Torsion. *Journal of Petrology*, 51(1–2), 21–42.  
635 <https://doi.org/10.1093/petrology/egp062>
- 636 Kohlstedt, D. L., & Holtzman, B. K. (2009). Shearing Melt Out of the Earth: An Experimentalist's  
637 Perspective on the Influence of Deformation on Melt Extraction. *Annual Review of Earth and  
638 Planetary Sciences*, 37(1), 561–593. <https://doi.org/10.1146/annurev.earth.031208.100104>

- 639 Kohlstedt, D. L., & Zimmerman, M. E. (1996). Rheology of Partially Molten Mantle Rocks. *Annual Review*  
640 *of Earth and Planetary Sciences*, 24(1), 41–62. <https://doi.org/10.1146/annurev.earth.24.1.41>
- 641 Lee, A. L., Walker, A. M., Lloyd, G. E., & Torvela, T. (2017). Modeling the impact of melt on seismic  
642 properties during mountain building. *Geochemistry, Geophysics, Geosystems*, 18(3), 1090–1110.  
643 <https://doi.org/10.1002/2016GC006705>
- 644 Long, M. D., & Becker, T. W. (2010). Mantle dynamics and seismic anisotropy. *Earth and Planetary*  
645 *Science Letters*, 297(3), 341–354. <https://doi.org/10.1016/j.epsl.2010.06.036>
- 646 Mainprice, D. (1997). Modelling the anisotropic seismic properties of partially molten rocks found at  
647 mid-ocean ridges. *Tectonophysics*, 279(1), 161–179. [https://doi.org/10.1016/S0040-](https://doi.org/10.1016/S0040-1951(97)00122-4)  
648 [1951\(97\)00122-4](https://doi.org/10.1016/S0040-1951(97)00122-4)
- 649 Miyazaki, T., Sueyoshi, K., & Hiraga, T. (2013). Olivine crystals align during diffusion creep of Earth’s  
650 upper mantle. *Nature*, 502(7471), Article 7471. <https://doi.org/10.1038/nature12570>
- 651 Paterson, M. S. (1990). Rock Deformation Experimentation. In *The Brittle-Ductile Transition in Rocks* (pp.  
652 187–194). American Geophysical Union (AGU). <https://doi.org/10.1029/GM056p0187>
- 653 Pec, M., & Al Nasser, S. (2021). Formation of Nanocrystalline and Amorphous Materials Causes Parallel  
654 Brittle-Viscous Flow of Crustal Rocks: Experiments on Quartz-Feldspar Aggregates. *Journal of*  
655 *Geophysical Research: Solid Earth*, 126(5), e2020JB021262.  
656 <https://doi.org/10.1029/2020JB021262>
- 657 Prior, D. J., Wheeler, J., Peruzzo, L., Spiess, R., & Storey, C. (2002). Some garnet microstructures: An  
658 illustration of the potential of orientation maps and misorientation analysis in microstructural  
659 studies. *Journal of Structural Geology*, 24(6), 999–1011. [https://doi.org/10.1016/S0191-](https://doi.org/10.1016/S0191-8141(01)00087-6)  
660 [8141\(01\)00087-6](https://doi.org/10.1016/S0191-8141(01)00087-6)
- 661 Qi, C., Hansen, L. N., Wallis, D., Holtzman, B. K., & Kohlstedt, D. L. (2018). Crystallographic Preferred  
662 Orientation of Olivine in Sheared Partially Molten Rocks: The Source of the “a-c Switch.”

- 663            *Geochemistry, Geophysics, Geosystems*, 19(2), 316–336.
- 664            <https://doi.org/10.1002/2017GC007309>
- 665    Quintanilla-Terminel, A., Dillman, A. M., Pec, M., Diedrich, G., & Kohlstedt, D. L. (2019). Radial Melt  
666            Segregation During Extrusion of Partially Molten Rocks. *Geochemistry, Geophysics, Geosystems*,  
667            20(6), 2985–2996. <https://doi.org/10.1029/2018GC008168>
- 668    Savage, M. K. (1999). Seismic anisotropy and mantle deformation: What have we learned from shear  
669            wave splitting? *Reviews of Geophysics*, 37(1), 65–106. <https://doi.org/10.1029/98RG02075>
- 670    Takei, Y. (2001). Stress-induced anisotropy of partially molten media inferred from experimental  
671            deformation of a simple binary system under acoustic monitoring. *Journal of Geophysical*  
672            *Research: Solid Earth*, 106(B1), 567–588. <https://doi.org/10.1029/2000JB900361>
- 673    Takei, Y. (2005). Deformation-induced grain boundary wetting and its effects on the acoustic and  
674            rheological properties of partially molten rock analogue. *Journal of Geophysical Research: Solid*  
675            *Earth*, 110(B12). <https://doi.org/10.1029/2005JB003801>
- 676    Takei, Y., & Holtzman, B. K. (2009a). Viscous constitutive relations of solid-liquid composites in terms of  
677            grain boundary contiguity: 1. Grain boundary diffusion control model. *Journal of Geophysical*  
678            *Research: Solid Earth*, 114(B6). <https://doi.org/10.1029/2008JB005850>
- 679    Takei, Y., & Holtzman, B. K. (2009b). Viscous constitutive relations of solid-liquid composites in terms of  
680            grain boundary contiguity: 2. Compositional model for small melt fractions. *Journal of*  
681            *Geophysical Research: Solid Earth*, 114(B6). <https://doi.org/10.1029/2008JB005851>
- 682    Takei, Y., & Holtzman, B. K. (2009c). Viscous constitutive relations of solid-liquid composites in terms of  
683            grain boundary contiguity: 3. Causes and consequences of viscous anisotropy. *Journal of*  
684            *Geophysical Research: Solid Earth*, 114(B6). <https://doi.org/10.1029/2008JB005852>

- 685 Takei, Y., & Katz, R. F. (2013). Consequences of viscous anisotropy in a deforming, two-phase aggregate.  
686 Part 1. Governing equations and linearized analysis. *Journal of Fluid Mechanics*, 734, 424–455.  
687 <https://doi.org/10.1017/jfm.2013.482>
- 688 Taylor-West, J., & Katz, R. F. (2015). Melt-preferred orientation, anisotropic permeability and melt-band  
689 formation in a deforming, partially molten aggregate. *Geophysical Journal International*, 203(2),  
690 1253–1262. <https://doi.org/10.1093/gji/ggv372>
- 691 Zhang, S., & Karato, S. (1995). Lattice preferred orientation of olivine aggregates deformed in simple  
692 shear. *Nature*, 375(6534), 774–777. <https://doi.org/10.1038/375774a0>
- 693 Zhang, S., Karato, S., Fitz Gerald, J., Faul, U. H., & Zhou, Y. (2000). Simple shear deformation of olivine  
694 aggregates. *Tectonophysics*, 316(1–2), 133–152. [https://doi.org/10.1016/S0040-1951\(99\)00229-](https://doi.org/10.1016/S0040-1951(99)00229-2)  
695 2
- 696 Zimmerman, M. E., Zhang, S., Kohlstedt, D. L., & Karato, S. (1999). Melt distribution in mantle rocks  
697 deformed in shear. *Geophysical Research Letters*, 26(10), 1505–1508.  
698 <https://doi.org/10.1029/1999GL900259>  
699  
700